Unconventional Direct Synthesis of Ni₃N/Ni with N-Vacancies for Efficient and Stable Hydrogen Evolution

*Doudou Zhang, Haobo Li,*Asim Riaz, Astha Sharma, Wensheng Liang, Yuan Wang, Hongjun Chen, Kaushal Vora, Di Yan, Zhen Su, Antonio Tricoli, Chuan Zhao, Fiona J. Beck, Karsten Reuter, Kylie Catchpole,* and Siva Karuturi**

Dr. Doudou Zhang, Ms. Astha Sharma, Dr. Wensheng Liang, Dr Fiona J. Beck, Dr. Di Yan, Prof. Kylie Catchpole and Dr. Siva Karuturi
School of Engineering, The Australian National University Canberra, ACT 2601, Australia

Dr. Haobo Li and Prof. Karsten Reuter
Theoretical Chemistry and Catalysis Research Center, Technische Universität München, Lichtenbergstr. 4, 85747 Garching, Germany

Dr. Yuan Wang, Dr. Zhen Su and Prof. Chuan Zhao
School of Chemistry, Faculty of Science, The University of New South Wales, Sydney, NSW 2052 Australia

Dr. Hongjun Chen and Prof. Antonio Tricoli
Nanotechnology Research Laboratory, Faculty of Engineering, University of Sydney, NSW 2006, Australia

Dr. Asim Riaz, Dr. Kaushal Vora and Dr. Siva Karuturi
Department of Electronic Materials Engineering, Research School of Physics, The Australian National University Canberra, ACT 2601, Australia

Prof. Karsten Reuter
Fritz-Haber-Institut der Max-Planck-Gesellschaft, Faradayweg 4-6, 14195 Berlin, Germany

E-mail: haobo.li@tum.de; kylie.catchpole@anu.edu.au; siva.karuturi@anu.edu.au;

Abstract

Transition metal nitrides are a fascinating class of catalyst materials due to their superior catalytic activity, low electrical resistance, good corrosion resistance and earth-abundance; however, their conventional synthesis relies on high temperature nitridation process in hazardous environments. Here, we report direct synthesis of Ni₃N/Ni enriched with N-vacancies using one-step magnetron sputtering. The surface state of Ni₃N (001) with 75% N-vacancies as hydrogen terminated exhibit four

inequivalent Ni_3-hollow sites. This leads to a lowest surface free energy (γ), strongest H* binding strength compared to Ni (111), and is affirmed as the most stable surface terminations under electrochemical working conditions (pH$\approx$13.8 and E = -0.1 eV) by a Pourbaix diagram. The Ni_3N/Ni catalyst shows low crystallinity and good wettability, and exhibits a low overpotential of 89 mV vs RHE at 10 mA cm^{-2} in 1.0 M KOH with an excellent stability of over 3 days. This performance closely matches with that of the Pt catalyst synthesized under the same conditions, and surpasses other reported earth-abundant catalysts on planar substrates. The application of Ni_3N/Ni as a cocatalyst on Si photocathodes produces an excellent ABPE of 9.3% and over 50 h stability. Moreover, its feasibility for practical application is confirmed with excellent performance on porous substrates and robustness at high operating currents in zero-gap alkaline electrolysis cells. Our work demonstrates a general approach for feasible synthesis of other transition metal nitride catalysts for electrochemical and photoelectrochemical energy conversion applications.

Introduction

Converting intermittent renewable energy to value-added chemicals (e.g., hydrogen, ethanol, and methanol) is a feasible strategy to address the issues of sustainable energy storage, transportation and consumption.[1] In particular, research on efficient production of green hydrogen through electrochemical water splitting using renewable electricity or photoelectrochemical (PEC) water splitting using sunlight has received tremendous attention in recent years. Central to these efforts is the development of high-performing earth-abundant catalysts with good operational stability for hydrogen evolution reaction (HER) and oxygen evolution reactions (OER) using scalable synthesis methods, which could allow the replacement of noble-metal catalysts such as Pt and Ir/Ru-based compounds in practical systems.[2, 3]

Ni-based compounds including oxides, sulphides, carbides, selenides and nitrides are highly attractive as HER catalysts due to their unique d-orbit electron configuration, earth-abundance and potential for low-cost synthesis.[4-8] Computations by Trasatti and Nørskov et al. have verified that hydrogen adsorption energies and exchange current densities of metallic Ni are close to that of Pt for the HER.[9, 10] Among the derivatives of Ni, Ni-nitrides and their heterostructures are particularly promising due to their high binding capabilities for the adsorbates (atomic hydrogen, protons, or water molecules) and relatively low electrical resistance.[11-13] Nevertheless, nitrides are usually synthesized by self-propagating high-temperature synthesis with nitridation at >400 °C in the presence of hazardous chemicals (such as azides, hydrazine, cyanamide, and ammonia) as the high strength of the N-N bonds hinders its direct synthesis.[12, 14, 15]

Reactive magnetron sputtering has been widely used as an industrial technique in preparing large area uniform thin films with high adhesion to the underlying substrates.[16] Monometallic and multimetallic electrocatalysts can be directly deposited onto target substrates with controlled loading amount and desirable composition.[17, 18] Similarly, cocatalyst layers can be deposited onto semiconductor

photoelectrodes in a clean vacuum environment without the risk of corrosion of the semiconductor materials as in solution-based synthesis. The structural properties of sputter deposited films can be controlled by adjusting the process parameters with good reproducibility. Moreover, catalysts with structural disorders and defects are shown to exhibit superior catalytic performance compared to their highly crystalline counterparts due to their high intrinsic activity from the abundant supply of active sites.[3, 19] For example, magnetron sputtering has been shown to generate oxygen vacancies due to the bombardment of energetic particles and the concentration of such defects plays an important role in achieving high activity.[20] Despite these advantages, there are no reports on the preparation of sputtered Ni-nitrides for electrochemical or PEC water splitting.

Crystalline-Si has revolutionized the photovoltaic industry due to its suitably narrow bandgap (~1.1 eV), high earth-abundance and availability of mature manufacturing technologies, and it has become a subject of intense research for PEC water splitting.[21] Various photoelectrodes have been successfully fabricated achieving high saturation photocurrent densities up to 40 mA cm^{-2}.[21-23] Cocatalysts on Si photoelectrodes play a crucial role in achieving high photovoltage as well as good operational stability. Given the chemical sensitivity of Si in alkaline solutions, compact metal-based cocatalysts could be employed both as a catalyst and a protection layer. These cocatalyst layers could effectively isolate the Si surface from corrosive electrolytes and avoid it being etched away by the solution. Therefore, it is of significance to develop sputtering deposition of cocatalysts for Si photocathodes, as it produces compact films which could protect Si from corrosion, and is performed via a vacuum process compatible with Si fabrication.

Herein, we report for the first time one-step synthesis of Ni$_3$N/Ni with triangular pyramid nanostructures using magnetron sputtering for the electrochemical and PEC HER in alkaline solution. In particular, the sputtered catalyst shows low crystallinity and N-vacancies with rich inequivalent N$_3$-hollow active sites, strong H* binding strength and superior electrochemical surface area. As a result,

the Ni₃N/Ni electrode presents an HER activity comparable to that of Pt electrodes with an overpotential of 89 mV at 10 mA cm^{-2}. Density-functional theory (DFT) calculations rationalize the important role of the N-vacancies for this high activity and stability from the low surface free energy (γ) and positive Bader charge values, and Surface Pourbaix diagram under working conditions. A Si photocathode with Ni₃N/Ni deposited as cocatalyst produces a current density of 38.8 mA cm^{-2} at 0 V vs reversible hydrogen electrode (RHE) with 0.59 V onset potential, an applied bias photon-to-current efficiency (ABPE) 9.3%, and with excellent durability over 50 h in strong alkaline media. In addition, the Ni₃N/Ni catalyst deposited on porous substrates produces remarkable performance and stability even at high current densities in zero-gap electrolyser cells demonstrating its feasibility for practical applications.

Results and Discussion

Sputtering deposition of Ni₃N/Ni and Ni₃N/Ni/Si photocathode preparation:
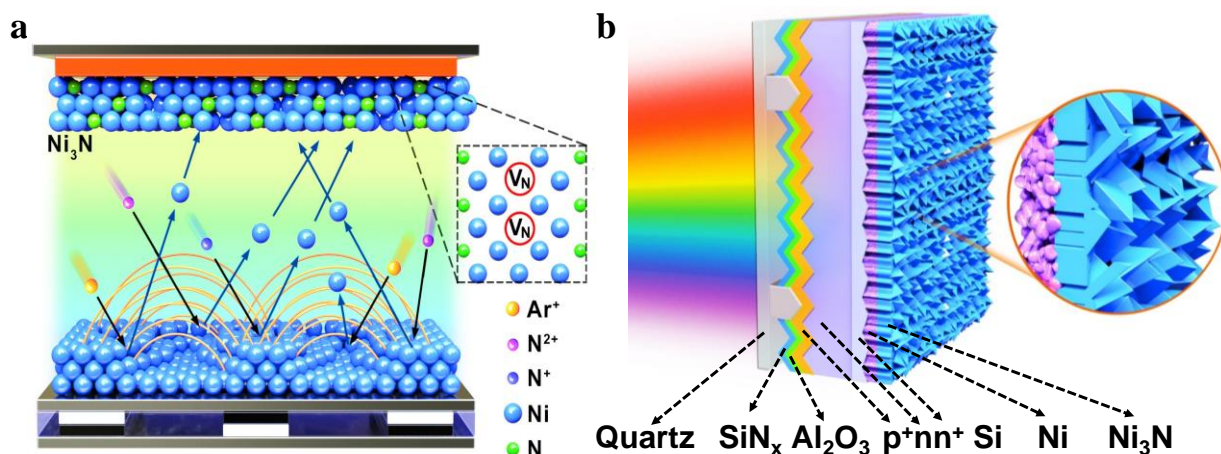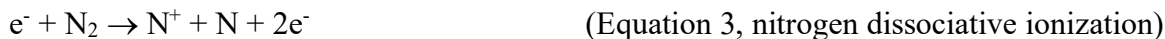

Fig. 1. (a) Schematic illustration of sputter deposition of Ni₃N films with N-vacancies. (b) Schematic illustration of the structure of Si photocathode consisting of a buried-junction Si coated with sputter-deposited Ni₃N/Ni cocatalyst.

To verify the synthesis of Ni₃N by magnetron sputtering and further optimize its HER activity, we first deposited Ni₃N films on fluorine-doped tin oxide (FTO) glass substrates using a Ni sputter target and nitrogen plasma. Nitrogen plasma includes molecular, atomic, and ionic nitrogen (N^{1+}and N^{2+}) species

5

which lead to the formation of N-vacancies.[24-26] Therefore, the formation of Ni_3N can be described using the following reactions:

$$e^- + N_2 \rightarrow N + N + e^- \qquad \text{(Equation 1, nitrogen dissociation)}$$

$$e^- + N_2 \rightarrow N_2^+ + 2e^- \qquad \text{(Equation 2, nitrogen ionization)}$$

$$e^- + N_2 \rightarrow N^+ + N + 2e^- \qquad \text{(Equation 3, nitrogen dissociative ionization)}$$

$$xNi + yN_2 \rightarrow Ni_xN_{2y} \qquad \text{(Equation 4, } Ni_3N \text{ formation)}$$

Considering that Ni_3N is an interstitial compound, nitrogen atoms occupy the octahedral interstitial sites of the Ni lattice in order to minimize the repulsive N-N interactions.[11, 27] The nitrogen species from dissociation and ionization of nitrogen atoms permeate into the Ni lattice resulting in the formation of Ni_3N with N-vacancies as illustrated in **Fig. 1a**. To evaluate the PEC performance of Ni_3N/Ni films as cocatalysts, Si photocathodes were fabricated with p^+nn^+ buried-junction structure as illustrated in Fig. 1b. Surface texturing was introduced with micropyramids on the front side and microgrooves on the rear side to minimize the reflection losses and enhance the catalytic active area, respectively. The front surface of the photocathodes was optimized for light harvesting and hole collection by depositing a pinhole-free Al_2O_3 (~10 nm) passivation layer, Si_3N_4 anti-reflection coating and Cr/Pd/Ag electrode grid. The rear surface was coated with Ni_3N/Ni cocatalyst film for hydrogen evolution in direct contact with alkaline electrolyte. More details of the fabrication process are provided in the experimental section in supporting information.

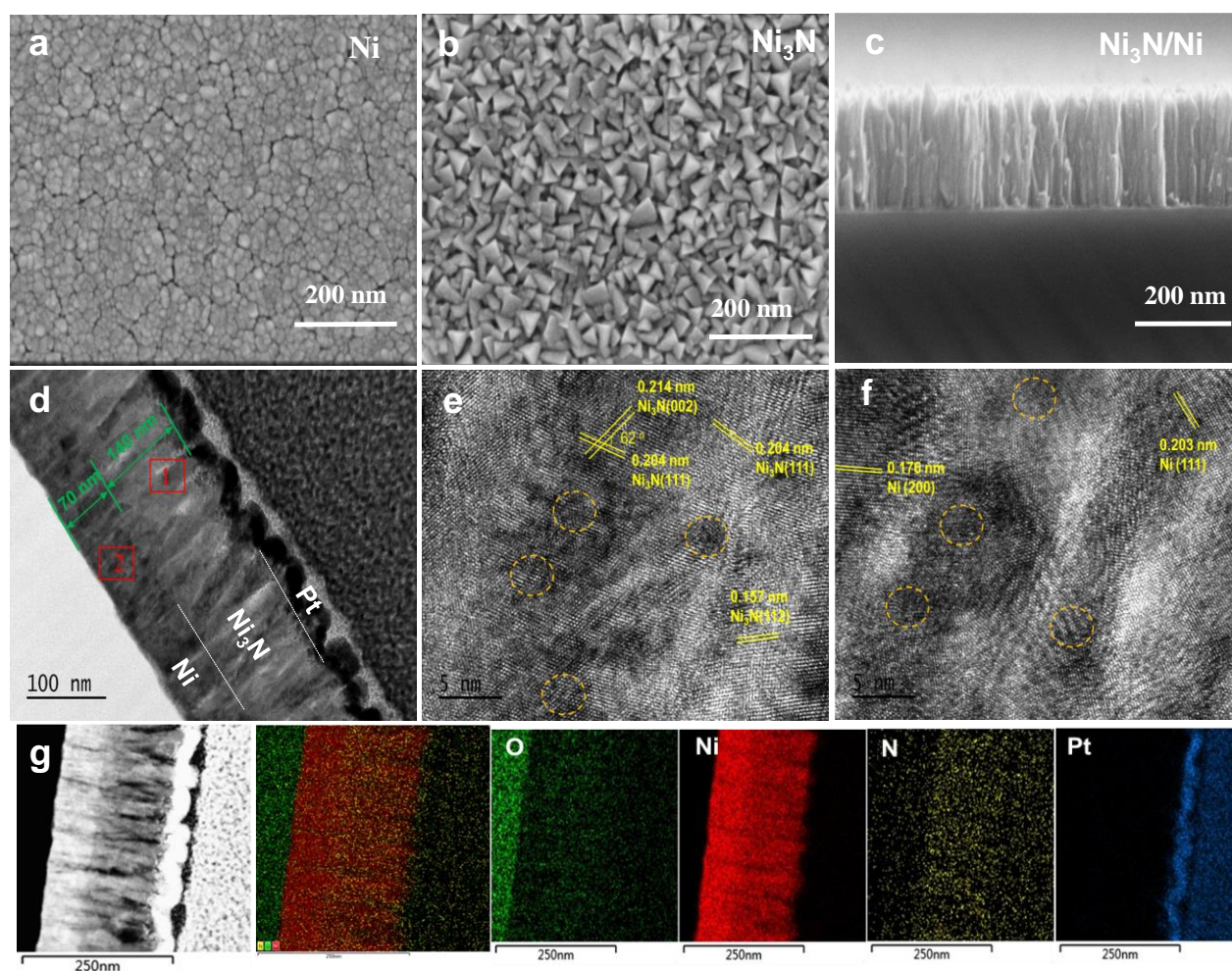**Synthesis and characterization of Ni_3N/Ni films:**

Fig. 2. Scanning electron microscopy images of (a) Ni and (b) Ni₃N from top-view, and (c) Ni₃N/Ni from cross-sectional view. (d) Scanning transmission electron microscopy image of Ni₃N/Ni layers with Ni₃N marked as block 1 and Ni marked as block 2. The Pt overlayer seen in Fig. 2d was added to protect the sample during the lamella preparation using focus ion beam (FIB). (e, f) High resolution transmission electron microscopy (HRTEM) images collected from blocks 1 and 2, respectively. (g) Transmission electron microscopy (TEM) image and the corresponding elemental mappings of Ni₃N/Ni. Pt observed in the images was deposited as a protection layer during the milling process for the preparation of cross-section samples.

Following a systematic study (described in the next section) of various Ni, Ni₃N and Ni₃N/Ni films on FTO glass substrates, the bilayer film consisting of ~140 nm of Ni₃N and ~70 nm of Ni deposited at 150 W direct current (DC) power presented best HER activity and was chosen for in-depth material characterizations. Because the surface roughness of FTO glass is relatively high, the thin films were deposited on mirror polished Si wafers coated with thick SiO_x for the purpose of material

characterizations. The individual Ni film shows a nanoparticle morphology with a feature size of ~20 nm with visible grain boundaries and cracks (**Fig. 2a**). The Ni_3N film shows triangular pyramid structure morphology (Fig. 2b) which is different from the Ni film and similar to that of the bilayer film (Fig. S1). No obvious cracks appeared in the Ni_3N film, which suggests that the film is stress-free. The cross-sectional images (Fig. 2c,d) of the bilayer film verify that it has hierarchical structure with ~140 nm-thick Ni_3N and ~70 nm-thick Ni.

The High Resolution Transmission Electron Microscopy (HRTEM) image of block 1 (Fig. 2e) shows disordered lattice fringes with inter-planar spacings of 0.204 and 0.214 nm, which are assigned to the (111) and (002) crystal planes of hexagonal Ni_3N with an intersection angle of 62°, respectively.[28, 29] The related selected area electron diffraction (SAED) pattern (Fig. S2a) with broad halos and sporadically located diffraction dots indicate low crystallinity of Ni_3N. The HRTEM and SAED of block 2 in Fig. 2f and Fig. S2b confirm the presence of (111) and (200) crystal planes of cubic Ni with inter-planar spacings of 0.203 and 0.178 nm, respectively, with low crystallinity indicated by the fuzzy and random lattice fringes.[30] In addition, the elemental mapping images of Ni_3N/Ni (Fig. 1g) show that Ni is homogeneously distributed in both the layers, while N is uniformly located in the Ni_3N layer. The Energy Dispersive X-ray (EDX) spectra in Fig. S3 confirm the presence of Ni and N as the major constituents.
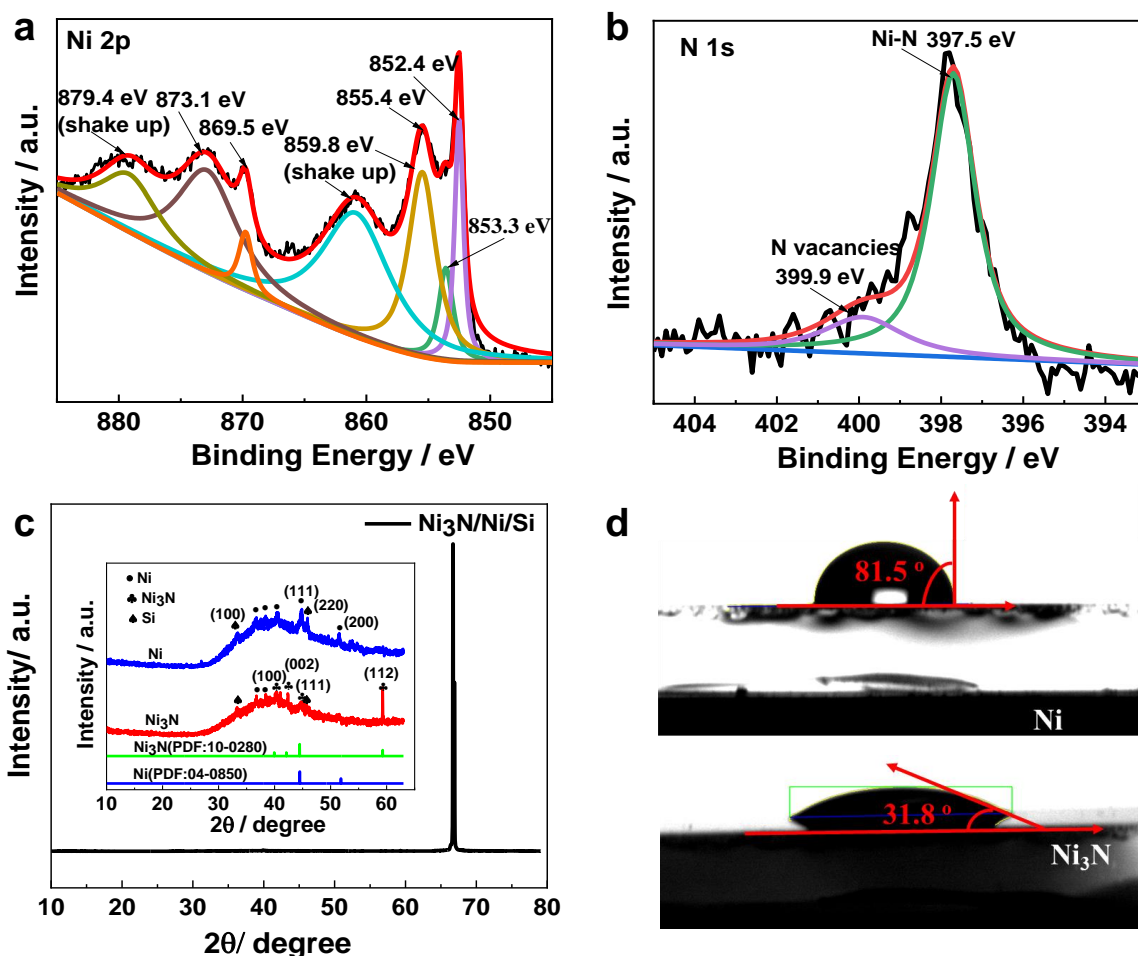
Fig. 3. (a) XPS spectra of (a) Ni 2p 3/2 and (b) N 1s of Ni_3N. (c) X-ray diffraction patterns of Ni_3N/Ni on Si wafer and the inset show the amplified XRD patterns of Ni and Ni_3N on Si wafer. (d) Water contact angle measurements for Ni/FTO and Ni_3N/Ni/FTO measured after resting water droplets on the surface for 4 s.

X-ray photoelectron spectroscopy (XPS) was performed to examine the composition of the Ni_3N film. From the Ni 2p XPS spectra (**Fig. 3a**), two peaks at 852.4 and 853.3eV are observed, which are assigned to metallic Ni and Ni(I) species of Ni_3N, respectively.[31-34] The peak at 855.4 eV is attributed to Ni^{2+} from surface oxidation, and the peak at 873.1 eV is assigned to metallic Ni.[30] The peak at 869.5 eV belongs to $2p_{1/2}$ of Ni^+, which is attributed to the presence of valence Ni^{1+} ($Ni^{<1+}$).[11] The predominance of $Ni^{<1+}$ in Ni_3N suggests that the electron density of a considerable fraction of Ni atoms is affected due to the existence of N-vacancies. The "shake up" satellites at the binding energies of

9

859.8 eV and 879.4 eV are also seen as significant Ni 2p peaks.[18] Furthermore, the N 1s XPS spectrum in Fig. 3b presents peaks at 397.5 and 399.9 eV, which are ascribed to N species of Ni_3N and the N-vacancies, respectively. The latter peak at 399.9 eV agrees with a similar observation made on oxide nanomaterials with oxygen vacancies.[35] In addition, detailed compositional analysis of XPS spectra reveals that the atomic ratio of Ni:N in Ni_3N is ~3.5:1, which is slightly nonstoichiometric due to the presence of N-vacancies in Ni_3N.

The X-ray diffraction (XRD) spectrum for Ni_3N/Ni/Si in the 2θ scan range of (10-80°) shows no discernible peaks of Ni and Ni_3N (Fig. 3c). Upon magnification in the range 10-60°, the Ni_3N spectrum shows weak and broad diffraction peaks attributable to hexagonal Ni_3N (JCPDS: 10-0280) accompanied by some noisy peaks, indicating poor crystallinity or defective structure of the material prepared by magnetron sputtering. There also exists peaks corresponding to Si (ICSD#96-901-1057).[36] Meanwhile, Ni prepared under the same conditions shows cubic structure with low crystallinity. These results agree well with the HRTEM observations (Fig.2e, f) and suggest that Ni_3N/Ni prepared by magnetron sputtering exhibits low crystallinity with disordered structure and N-vacancies.

We further measured the water contact angles on Ni/FTO and Ni_3N/FTO samples. The surface wettability of an electrocatalyst indicates the surface adsorption of water molecules and the interaction of the catalyst with electrolyte, thereby plays an important role in electrocatalytic activity. The much smaller contact angle on Ni_3N/FTO as illustrated in Fig. 3d suggests a higher wettability for Ni_3N/Ni/FTO due to hydrophilic Ni-N bonds on the surface, which could be beneficial for enhanced HER kinetics.[37]

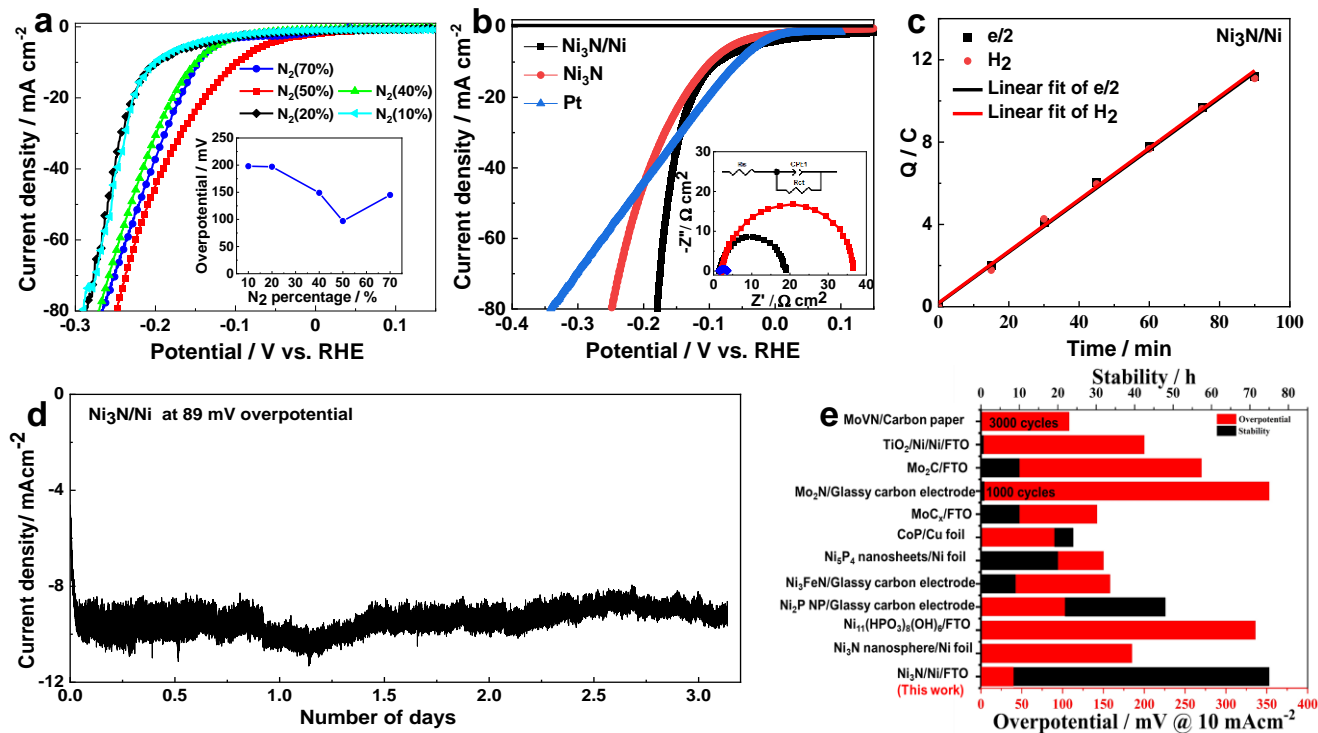**Electrochemical performance of Ni_3N/Ni films:**

Fig. 4. (a) LSV curves (with 90% iR-compensation) of Ni_3N/FTO electrodes sputtered under different N_2: Ar flows. The flow of Ar carrier gas was fixed at 20 sccm. The inset summarizes the overpotential at 10 mA cm^{-2} for different N_2: Ar flows. (b) LSV curves (with 90% iR-compensation) of Ni_3N/Ni, Ni_3N, and Pt on FTO substrates and the corresponding Nyquist plots (inset in Fig. 3b). (c) H_2 (red dots) evolved from the Ni_3N/Ni cathode detected by gas chromatography and the calculated amounts of H_2 (black dots). The measurement was performed at j_{HER}=10 mA cm^{-2}. (d) Chronoamperometry measurement of the Ni_3N/Ni for HER at an overpotential of 89 mV in 1.0 M KOH. (e) Comparison of the overpotential and stability of Ni_3N/Ni for the HER with the other reported earth-abundant catalysts on planar substrates at a current density of 10 mA cm^{-2}.

The electrocatalytic performance of Ni_3N based electrodes towards the HER was evaluated in 1.0 M KOH electrolyte (pH=14) saturated with N_2 gas. The sputtering power and the thickness of Ni_3N were first optimized based on the HER overpotential of the deposited films on FTO glass substrates at 10 mA cm^{-2} current. As shown in Fig. S4 in the supplementary information, the Ni_3N/Ni synthesized at 150 W presents the best activity with lowest overpotential. Similarly, Ni_3N presents the lowest

11

overpotential when the sputtering duration was fixed at 1000 s (Fig. S5), which suggests that a further increase in Ni_3N film thickness hinders its catalytic kinetics.

To understand the relationship between the synthesis conditions and N-vacancies, we varied the N_2: Ar gas ratio in the sputtering chamber while keeping the Ar carrier gas flow rate constant. We also assessed their respective performances for the HER using linear sweep voltammetry (LSV) measurements as shown in **Fig. 4a**. The LSV data confirms that the Ni_3N sputtered under 50% N_2: Ar gas ratio outperforms the other electrodes. As confirmed by the overpotentials at 10 mA cm^{-2} current as shown in the inset in Fig. 4a, the HER performance worsened when the ratio is either increased or decreased. Fig. S6 shows the XPS spectra of N 1s of Ni_3N catalysts synthesized under different gas ratios. When the N_2: Ar ratio was 70%, stoichiometric Ni_3N was obtained with an atomic ratio of 3:1. With the decreasing gas ratio, the atomic ratio departed gradually from the stoichiometric ratio. When the ratio is below 10%, no N signal was detected, indicating a deposition of pure Ni with Ni-termination. However, N-vacancies first increased with the decreasing gas ratio until 40% as indicated by the area of the peak at 399.9 eV^{11}, and then decreased with a further decrease in the gas ratio due to the appearance of metallic Ni. Accordingly, the Ni-N peak position shifted to a lower position first and then to a higher position due to the change in the position of the *d*-band centre of Ni_3N by the presence of N-vacancies.[38-40] The superior performance of Ni_3N deposited under 50% N_2: Ar ratio is likely due to an optimal synthesis condition which could in turn result in an optimal N-vacancy concentration as further explained in the later section using DFT calculations.

As Ni is often used as a substrate material to prepare high performance heterostructured catalysts, we also investigated the effect of Ni inclusion by preparing Ni_3N/Ni bilayer electrodes. Pt, known as the best HER catalyst, was also sputtered on FTO for comparison. The LSV obtained for different electrodes for the HER in 1.0 M KOH are shown in Fig. 4b. The $Ni_3N/Ni/FTO$ electrode exhibits a commendable HER performance presenting low overpotentials of only 89 and 155 mV at 10 and 40

mA cm^{-2}, respectively. In comparison, the Pt/FTO electrode requires corresponding overpotentials of 57 and 169 mV to deliver the same HER current densities. It is noted that low overpotential at 40 mA cm^{-2} current density is particularly beneficial for PEC hydrogen generation on Si photocathodes. Interestingly, the addition of Ni film significantly enhances the performance of sputtered Ni$_3$N films. Compared to the Ni$_3$N/FTO electrode, the Ni$_3$N/Ni/FTO electrode shows a reduction in overpotential at 40 mA cm^{-2} by ~30 mV (see Fig. S7). This drastic improvement in the HER activity could be attributed to the synergistic effect of Ni$_3$N and Ni which could enhance the electronic conductivity and relieve the film stress, thereby improving the HER performance. For example, a similar observation was reported for hematite deposited on FTO substrates, which resulted in lattice strain between the hematite and the substrate. The lattice strain was addressed by adding a thin layer of other materials at the interface.[41]

The Tafel plots of the electrodes (see Fig. S8) derived from the polarization curves in Fig. 4b confirm that Ni$_3$N/Ni/FTO (38 mV dec^{-1}) has much lower slope compared to Ni$_3$N/FTO (60 mV dec^{-1}), but only slightly higher than that of Pt/FTO (28 mV dec^{-1}). Since the Tafel slope of an electrocatalyst is an indication of its HER reaction kinetics,[42, 43] the lower Tafel slope of Ni$_3$N/Ni/FTO illustrates that the bilayer catalyst possesses faster kinetics and superior catalytic activity.

To further analyze the HER performance of different electrodes, electrochemical impedance spectroscopy (EIS) was carried out. As shown by the Nyquist plots in the inset in Fig. 4b, Ni$_3$N/Ni/FTO presents a much smaller charge transfer resistance (R$_{ct}$) at the electrode-electrolyte interface compared to Ni$_3$N/FTO (16.19 vs 33.47 Ω cm^{-2}, Table S1), illustrating an enhanced charge transport upon the addition of Ni layer. In order to assess the specific intrinsic activities of Ni$_3$N/Ni/FTO and Ni$_3$N/FTO, their electrocatalytic activities were normalized by the electrochemically active surface area (ECSA) measured by the double layer capacitance method on the basis of cyclic voltammetry in 1.0 M KOH electrolyte (Fig. S9). The higher double layer capacitance (C$_{dl}$) of Ni$_3$N/Ni/FTO (1.10 mF cm^{-2}) compared to that of Ni$_3$N/FTO (0.65 mF cm^{-2}) indicates that

Ni$_3$N/Ni/FTO possesses a higher ECSA.[3, 44, 45] This further confirms that the inclusion of the Ni layer plays a key role in boosting the catalytic activity of Ni$_3$N films.

The Faradaic efficiency measurements (Fig. 4c) of the Ni$_3$N/Ni cathode based on the measured and calculated amounts of the evolved H$_2$ gas prove that there were no undesirable side reactions. To further examine the durability of Ni$_3$N/Ni/FTO as a cathode, a fixed overpotential of 89 mV was applied. As shown in Fig. 4d, a stable cathodic current density of ~10 mA cm^{-2} was maintained for over 3 days with negligible degradation, demonstrating its remarkable stability in alkaline medium. In addition, as summarized in Fig. 4e and Table S2, the hierarchical Ni$_3$N/Ni/FTO exhibits the smallest overpotential and superior stability at 10 mA cm^{-2} among other earth-abundant alkaline catalysts reported thus far on planar substrates. These results confirm that the sputtered Ni$_3$N/Ni films not only exhibit exceptionally high HER catalytic activity which closely matches Pt, but also robust electrochemical stability for practical applications.
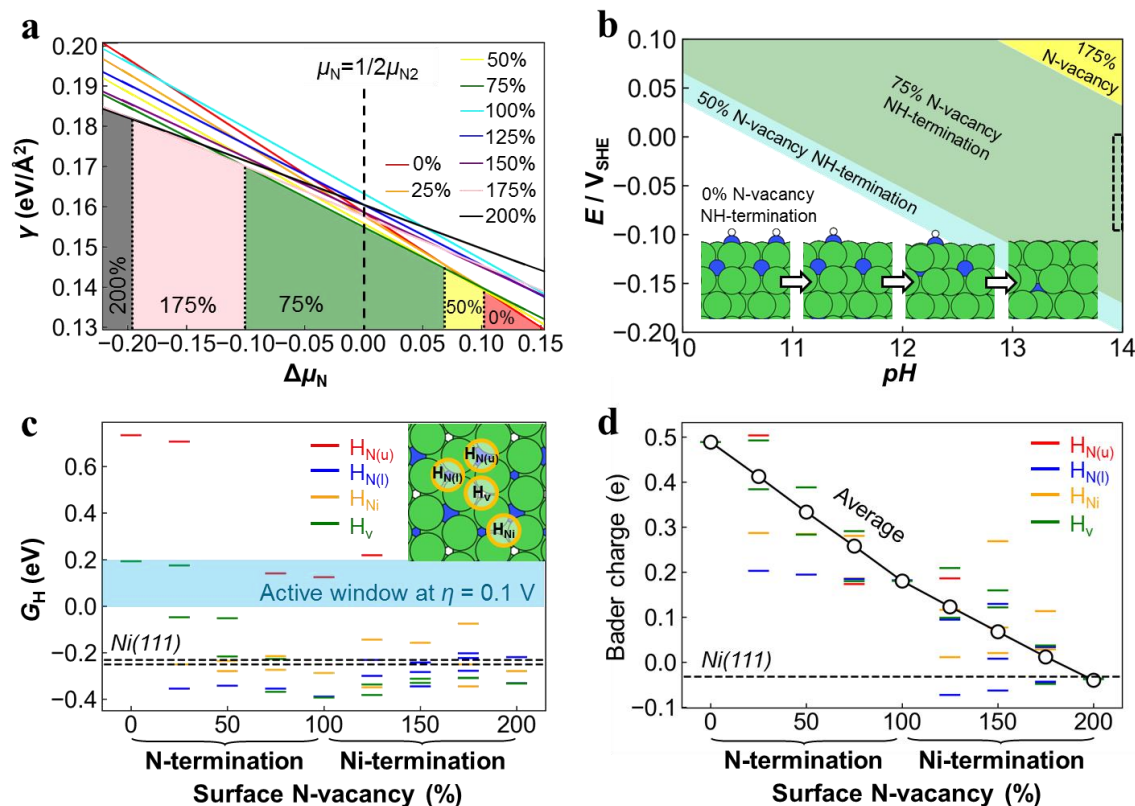
Density-functional theory calculations:

Fig. 5. (a) Surface free energy (γ) of Ni$_3$N(001) with a varying amounts of N-vacancies as a function of surface chemical potential difference to gaseous N$_2$ ($\Delta\mu_N$). N-vacancy concentration of 0%-100% corresponds to the vacancies of the surface layer, and 100%-200% to the sub-surface layer. The coloured areas show the region of most stable structures under the lines with lowest γ. Black, pink, green, yellow and red lines correspond to combined N-vacancy concentrations in the surface and sub-surface layer of 200% (Ni), 175%, 75%, 50% and 0% (Ni$_3$N), respectively (atomic structures are shown in Fig. S10). 75% N-vacancy concentration is most stable at gaseous N$_2$ conditions (horizontal black dashed line). (b) Surface Pourbaix diagram of Ni$_x$N$_y$H$_z$ with N with reference to dissolved N$_2$. The HER working condition is 1.0 M KOH (pH≈13.8) and E = -0.1 eV, as approximately marked in the black dashed box. (c) Adsorption free energies of H* (G_H) on 4 inequivalent Ni$_3$-hollow sites exhibited by a Ni$_3$N(001) surface with varying degree of surface N-vacancies. Multiple data points of the same colour correspond to the non-equivalent sites with different distances to surface N. The G_H on the inequivalent 2 Ni$_3$-hollow sites offered by Ni (111) are marked as horizontal dashed lines for comparison. The high HER activity region (G_H within 0-0.2 eV) is marked in light blue, see the text. (d) Bader charge of 4 inequivalent Ni$_3$-hollow sites exhibited by a Ni$_3$N (001) surface with varying degree of surface N-vacancies. Positive Bader charge values represent atoms with positive charge. The corresponding values for the Ni$_3$-hollow sites at Ni (111) are shown as dashed lines for comparison (the

two inequivalent sites share the same value). The average values of the surface Ni atoms for each termination are marked as circles.

DFT calculations were performed to understand the surface structure and the origin of the high activity of Ni_3N/Ni. The $Ni_3N(001)$ is a flat metallic surface and can be either N- or Ni-terminated. The Ni_3N (001) facet is chosen for calculation, which is the same surface as the (002) facet observed in both TEM images (Fig. 2e) and XRD patterns (Fig. 3c). To simulate the effect of surface N-vacancies, the N-terminated and Ni-terminated surfaces are defined as 0% and 100% N-vacancy, respectively, while the surface also depleted of sub-surface N is defined as 200% N-vacancy (see also Fig. S10). Based on this, a series of surface structures with gradual concentrations of N-vacancies from 0% to 200% were constructed, which also include NH-terminated surfaces in the aqueous conditions. The corresponding surface free energies (γ) were calculated to identify the most stable surface structures of $Ni_3N(001)$ under both the synthesis and operating conditions. As shown in **Fig. 5a**, γ is related to the chemical potential for N (μ_N). With μ_N decreases to be more negative, the concentration of N-vacancies of the most stable surface structure with lowest γ (marked in colored regions) increases gradually from 0% to 200%. In N_2 atmosphere as representative of the synthesis process, the surface with 75% N-vacancies is the most stable. To further relate the surface structure to the experimental HER working condition, a Pourbaix diagram of the most stable surface terminations among the whole range of 0-200% N-vacancy concentrations with possible *N or *NH surface terminations as a function of the working potential (E) and the pH value is calculated as shown in Fig. 5b. As marked by black dashed square, under pH≈13.8 and E = -0.1 eV in aqueous solution, the surface with 75% N-vacancies is the most stable, but it is hydrogen terminated. N-vacancies are thus found to be strongly enriched at the surface, which agrees with the XPS characterization results in Fig. 3.

The $Ni_3N(001)$ surface with or without N-vacancies is metallic, as evidenced by the finite projected density of states (pDOS) around the Fermi level as shown in Fig. S11. As judged from the pDOS shape, the 75% N-vacancy $Ni_3N(001)$ surface resembles a regular Ni(111) surface. This shows that the surface

is electrically conducting and the standard descriptor to assess HER activity on transition metal surfaces, the H adsorption free energy (G_H), could also be employed here. From a thermodynamic point of view, optimum HER activity is achieved at $G_H \sim 0$ eV.[46, 47] According to a recently proposed model of overpotential influence on the volcano line,[48] the working overpotential (η) of +0.1 V shifts the high HER activity region to ~0-0.2 eV. DFT calculations were carried out to determine G_H on a variety of adsorption sites of $Ni_3N(001)$. Especially the Ni_3 sites (hollow sites formed by three surface Ni atoms) offered by the $Ni_3N(001)$ surface are found to be similar to those on Ni(111), and are thus suggested as potentially active sites for the HER. There are 4 such inequivalent Ni_3-hollow sites (see inset in Fig. 5c): one above a lower-layer N ($H_{N(l)}$), one above an upper-layer N($H_{N(u)}$), one above a Ni atom (H_{Ni}) and one on the pore without sub-surface atoms (H_v). Each site type can have two or three different configurations when N-vacancies are present at the surface.

In order to avoid the risk from the insufficient representation of the selected site structure, a systematic computational screening of all active-site motives has been performed to achieve a general trend to present the performance of the catalyst.[49] As shown in Fig. 5c, the adsorption free energies of the intermediate H*(G_H) exhibit a general decrease trend with increasing N-vacancy concentration, indicating an increase of the H* binding strength at the $Ni_3N(001)$ surface. In the limit of a pure Ni-termination (200% vacancy), the binding then essentially resembles the one of a regular Ni(111) surface with G_H around -0.25 eV. Intriguingly, at around 75-100% N-vacancy concentration, i.e., at the surface termination identified as most stable under HER working conditions, significantly weaker binding is possible at the $H_{N(u)}$ site that then falls exactly into the high HER activity window. On this basis, higher HER activity than of regular Ni(111) would be expected, consistent with the measured higher HER performance in Fig. 4b.

In order to further understand the origin of the different binding strength of H* on surfaces with N-vacancies, the *d*-band center position (Fig. S12) and Bader charge (Fig. 5d) of the four inequivalent

Ni$_3$-hollow sites were calculated. While there is a considerable spread over the four sites for each termination, there are trends in the average values of the d-band center position and Bader charge of the surface Ni atoms. With increasing N-vacancy concentration, the d-band center position first increases and then decreases, whereas the Bader charge decreases monotonously. Therefore, compared to the d-band center, the Bader charge value is more appropriate to explain the influence of the surface N-vacancy concentration on the catalytic performance of the surface Ni atoms. For the most stable 75-100% N-vacancy termination with optimum HER activity the d-band position is Ni-like, while the average Bader charge at the active sites is still positive at about 0.2, i.e., the Ni atoms transfer charge to the N atoms to keep the surface positively charged. Compared with the Ni(111) surface where Ni atoms have almost zero charge, the electron deficient sites on Ni$_3$N allow a weakened H bonding with higher HER activity. Instructively, for Ni-based catalysts due to the strong binding between Ni and H atoms, adjusting the content of non-metallic atoms appropriately to make the surface atoms have an average positive charge of about 0.2 could achieve an optimal HER catalytic activity. This could be employed as a general strategy to design Ni-based catalysts with high activity.

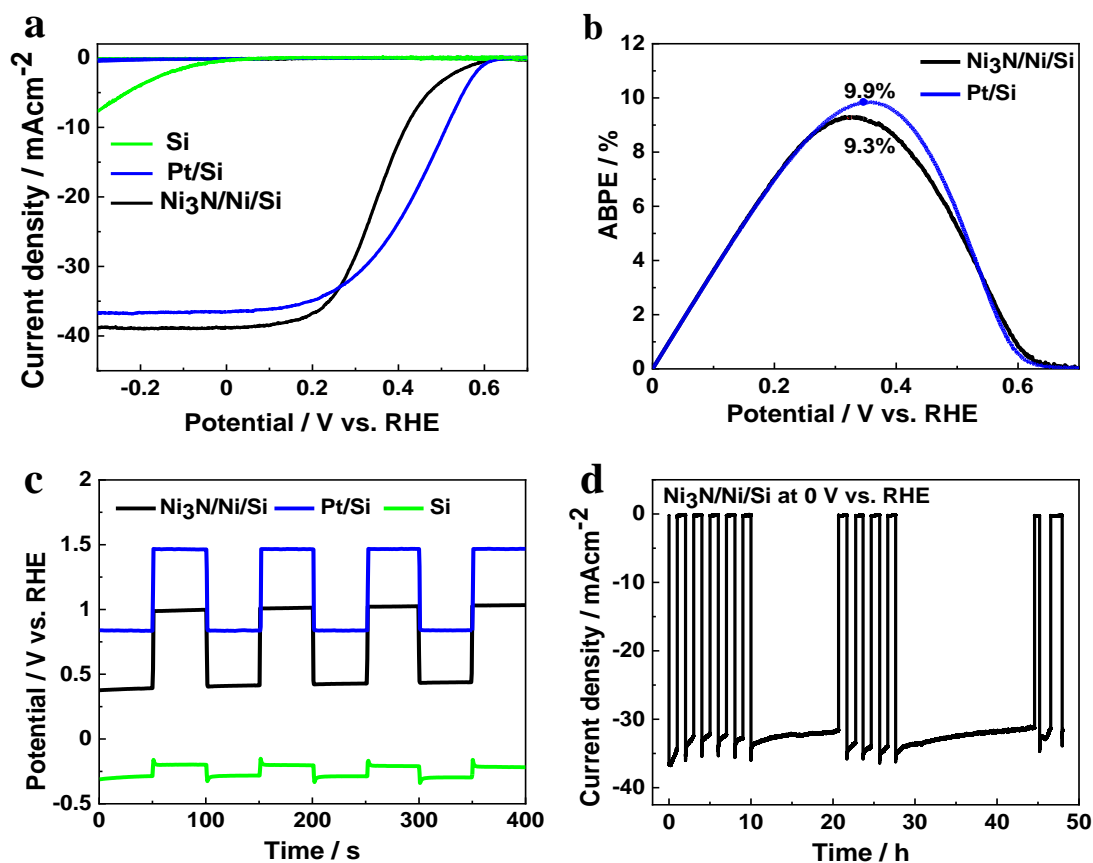**Photoelectrochemical characterization of Ni$_3$N/Ni/Si photocathodes:**

Fig. 6. (a) Linear sweep voltammetry of Si, Pt/Si and Ni₃N/Ni/Si photocathodes and (b) the corresponding applied bias-to-photon current conversion efficiency, and (c) Open-circuit potential plots. (d) Chronoamperometry measurements for the Ni₃N/Ni/Si photocathode at 0 V vs. RHE. All the measurements were performed at 0 V vs. RHE in 1.0 M KOH electrolyte (pH=14) under AM1.5G illumination (100 mW cm^{-2}).

To evaluate the performance of sputter deposited Ni₃N/Ni as a cocatalyst for PEC water splitting, LSV measurements of Si, Pt/Si and Ni₃N/Ni/Si photocathodes were conducted in a three-electrode system, illuminated from the front p$^+$ side. As shown in **Fig. 6a**, the Si photocathode without any cocatalyst presents a low onset potential below the thermodynamic HER potential of 0 V vs RHE, rendering it ineffective for water splitting. In contrast, the photocathodes modified with Pt and Ni₃N/Ni catalysts show much improved performances. The Ni₃N/Ni/Si photocathode exhibit an onset potential at 0.59 V and a photocurrent density of 38.8 mA cm^{-2} at 0 V vs RHE. In comparison, Pt/Si delivers a slightly lower photocurrent density of 36.5 mAcm^{-2} with a similar onset potential. Fig 6b shows that Ni₃N/Ni/Si

19

displays an ABPE of 9.3% which is comparable to that of the Pt/Si photocathode (9.9%), suggesting that Ni_3N/Ni co-catalyst is a superior choice to construct low-cost photocathodes.

To further understand the positive shift of onset potential for the as-prepared electrodes, open circuit potentials (OCP) were measured in the dark and under illumination as shown in Fig. 6c. The OCPs for the samples move towards higher potentials upon exposure to the incident light which is caused by the formation of a built-in electric field. The OCP differences before and after illumination are 0.1, 0.60, and 0.64 and for the Si, Ni_3N/Ni/Si and Pt/Si photocathodes, respectively, which corresponds well with their onset potential values. Evidently, the integration of the Ni_3N/Ni and Pt cocatalysts greatly enhances the transfer of photogenerated holes toward the substrate, thereby delivering high photovoltages. The wavelength dependent incident photon-to-current conversion efficiency (IPCE) for Ni_3N/Ni/Si photocathode (Fig. S13) measured at 0 V vs RHE in the wavelength range of 300-1200 nm reveals a good light harvesting ability of the photocathode at energies above the bandgap of Si. The stability measurement (Fig. 6d) over 50 h under simulated one sun illumination indicates that the Ni_3N/Ni catalyst film effectively stabilizes Si photocathodes in alkaline solutions. On the other hand, the Si photocathode without any cocatalysts gets etched by the solution immediately (Fig. S14). These results confirm that the sputtered Ni_3N/Ni film serves not only as a high-performance cocatalyst for Si photocathodes, but also as an excellent protection layer in alkaline media.

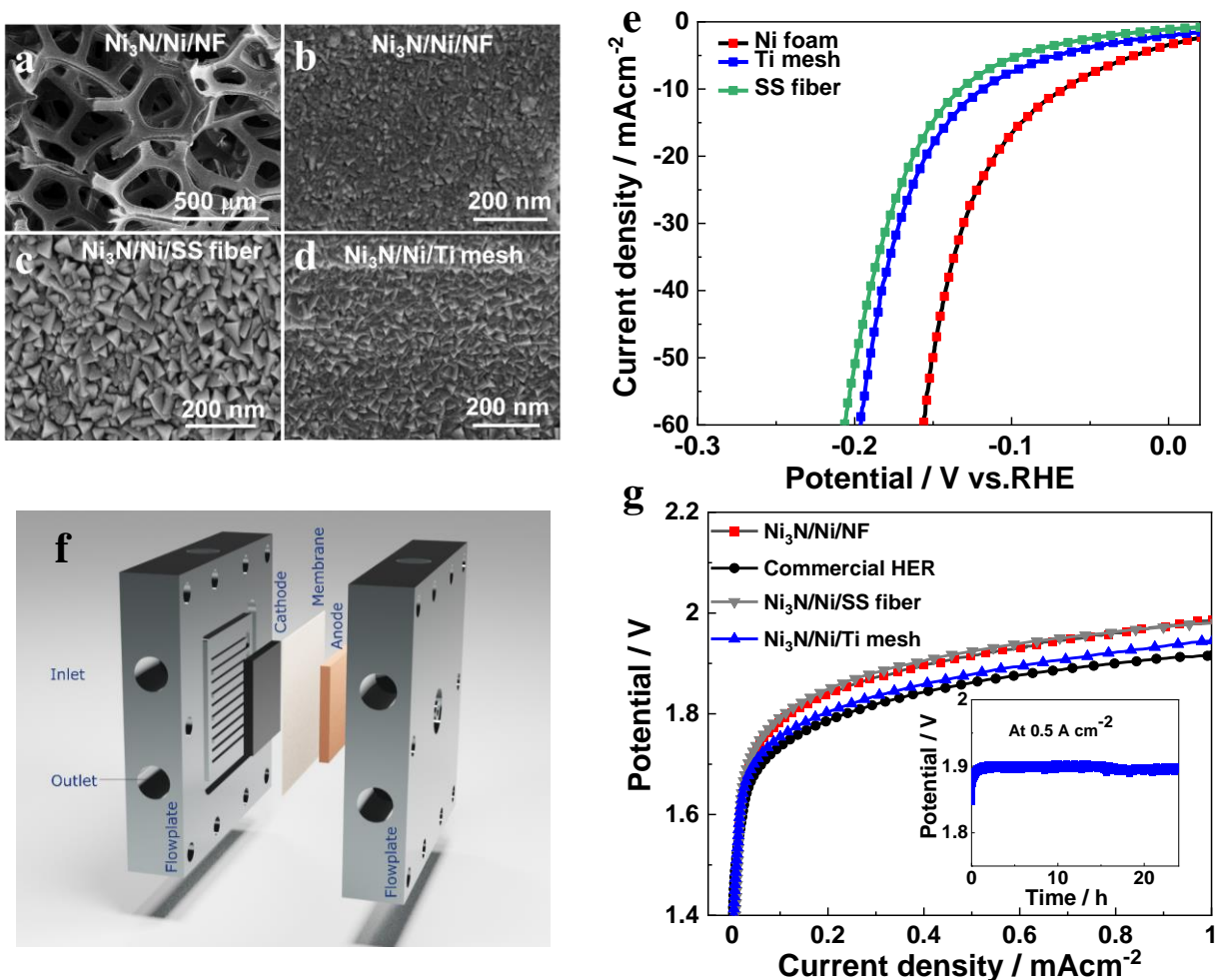**Ni_3N/Ni on porous substrates and application in zero-gap cells:**

Fig. 7. (a-d) SEM images of Ni$_3$N/Ni on different porous substrates. (e) LSV curves (with 90% iR-compensation) of Ni$_3$N/Ni on Ni foam (NF), Ti-mesh, stainless steel (SS) fiber substrates in 1.0 M KOH. (f) Schematic illustration of the configuration of the zero-gap electrolyser cell employed to test the performance at high current densities. (g) Current vs voltage plots for the zero-gap alkaline water electrolyser with different Ni$_3$N/Ni porous electrodes as cathodes and NiFe$_2$O$_4$ as anode separated by Fumapem FA-3-50 anionic membrane in 1.0 M KOH at 55 °C. Inset the long-term stability of the Ni$_3$N/Ni/Ti-mesh electrode in the zero-gap cell.

In order to evaluate the performance of Ni$_3$N/Ni catalyst on porous substrates and at high current densities relevant to practical application, we fabricated Ni$_3$N/Ni catalysts on different porous substrates, including Ni foam (NF), Ti mesh and stainless steel fiber, and evaluated their performance in zero-gap alkaline water electrolysis cells. The substrates were cleaned following the procedure as described in the experimental section in the supporting information. Ni$_3$N/Ni was sputtered on different

21

porous substrates using the synthesis conditions optimized on FTO substrates. This is expected to yield a similar thickness except for small changes due to variation in the surface structure of different porous substrates. From the SEM images of the blank substrates (Fig. S15a-c), it is clear that different porous substrates present different surface characteristics. Among them, SS fiber presents a flatter and smoother surface except for the rubbed surface, which is comparable to that of planar FTO substrate. On the other hand, Ti mesh and NF present rough and uneven surfaces. Upon the catalyst coating, there is no obvious change in the surface morphology from the SEM images collected at low magnification (Fig. 7a, Fig. S15d-e). This indicates that sputter deposition results in a compact coating of catalyst layers on porous substrates with no aggregation. From the SEM images collected at higher magnification (Fig. 7b-d), obvious surface features can be noticed. Ni_3N/Ni shows a similar triangular pyramid structure on all the porous substrates. However, the size of the structures varies among different substrates, which is due to the difference in their surface properties. Noticeably, the morphology of Ni_3N/Ni on SS fiber is almost identical to that on FTO substrates due to its flatter and smoother surface.

The electrochemical performance of the different porous electrodes was examined using LSV measurements in three-electrode system in 1.0 M KOH. As shown in Fig. 7e, the $Ni_3N/Ni/NF$ electrode outperforms the other porous electrodes presenting ~66 mV overpotential at 10 mA cm^{-2}. In comparison, the Ni_3N/Ni on SS fiber and Ti-mesh presents 132 and 118 mV overpotentials, respectively. It is noted that the overpotential on NF is even lower than that observed on FTO which is due to its large interfacial surface area. In addition, $Ni_3N/Ni/NF$ shows excellent electrochemical stability as indicated by nearly constant overpotential at 15 mA cm^{-2} for 139 hours (Fig. S16a). The LSV data of $Ni_3N/Ni/NF$ collected before and after the stability test shows negligible change (Fig. S16b). These results confirm that our Ni_3N/Ni catalyst with N-vacancies directly synthesized using reactive magnetron sputtering presents promising HER performance even on porous substrates which

also compares favorably among other porous Ni nitrides reported in the literature (Table S3). The Nyquist plots from the EIS measurements (Fig. S17, Table S4) confirm that Ni_3N/Ni SS fiber electrode presents the largest semicircle and the highest charge transfer resistance (26.28 Ωcm^2) among all the electrodes, which results in a low HER performance.

To observe the performance of Ni_3N/Ni at high current densities for overall water splitting, we designed zero-gap cells as illustrated by the schematic in Fig. 7f. Further details on the zero-gap cell configuration are provided in the experimental section. Commercially-available NiCoFe on Ni fiber (cathode) and $NiFe_2O_4$ on stainless steel fiber (anode) were obtained from Dioxide Materials Inc. and used them as reference.[50] The performances of the commercial electrodes for the HER and OER in three-electrode configuration are presented in Fig. S18. In all the zero-gap cell measurements, the $NiFe_2O_4$ electrode was used as anode and the cell was stabilized at 0.25 A cm^{-2} for 1 h prior to recording the response.

It can be seen that water electrolysis commences at a cell voltage >1.65 V and very high current densities are achieved with increasing cell voltages. The cell voltages for current densities of 0.5 A cm^{-2} for Ni_3N/Ni on Ti-mesh, SS fiber and NF are ~1.88 V, 1.90 V and 1.92 V respectively, which is approximate to the performance of commercial NiCoFe electrode with 1.85 V. It is interesting to note that the Ni_3N/Ni on NF does not show any superiority in the performance in the zero-gap cell different to its performance in three-electrode measurements at low current densities. We attribute this to the relatively low through-plane conductivity of the NF substrate compared to the other porous substrates resulting in voltage losses at high current densities as confirmed by the EIS data (Fig. S19, Table S5). On the other hand, the Ni_3N/Ni on Ti-mesh show comparable performance with that of the commercial HER electrode. Ti mesh presents high through-plane conductivity and supports efficient bubble dissipation through its 2D porous structure, thereby outperforming the other porous electrodes in zero-gap cells. The performance also compares favorably to the other reported Ni-based electrodes in single

cell water electrolysis cell (Table S6). The long-term performance the Ti-mesh electrode in the zero-gap cell shown as inset in Fig. 7g confirm that it maintains stable activity even at very high operating currents. In summary, the performances on various porous substrates and in zero gap alkaline water electrolysis cells confirm the feasibility of sputtered Ni_3N/Ni with N-vacancies as a highly versatile HER electrocatalyst with a potential for practical application.

Conclusions

A hierarchical catalyst comprising pyramidal structured Ni_3N/Ni with N-vacancies was directly synthesized by reactive magnetron sputtering for alkaline hydrogen evolution reaction. Due to a synergistic enhancement of N-vacancies, high wettability, and high electrochemical surface area, the Ni_3N/Ni bilayer catalyst presents excellent activity together with a remarkable stability. DFT calculations demonstrated that 75% N-vacancies concentration on the surface lead to the superior activity and stability under strong alkaline media. Different to $Ni(111)$, such $Ni_3N(001)$ surfaces with N-vacancies exhibit metallic properties, lower surface free energy, positive charge sites and stronger H^* binding strength under electrochemical working conditions. The Ni_3N/Ni decorated as a cocatalyst on Si photocathodes enhances its onset potential to 0.59 V, achieving 9.3% applied-bias photon-to-current conversion efficiency with high operational stability. Moreover, commendable performances and robustness were observed on porous substrates and at high current densities in zero-gap alkaline electrolysis cell. The demonstration of earth-abundant Ni_3N/Ni catalysts with superior HER performance, and one-step synthesized using reactive magnetron sputtering, i.e., without the need of a high temperature nitridation process, provides a general approach for the fabrication of transition metal nitrides for electrochemical and photoelectrochemical hydrogen production.

Supporting Information

Supporting Information is available from the journal or from the author.

Conflicts of interest

There are no conflicts to declare

References

1. N. S. Lewis and D. G. Nocera, *Proceedings of the National Academy of Sciences*, 2006, **103**, 15729-15735.
2. I. Roger, M. A. Shipman and M. D. Symes, *Nature Reviews Chemistry*, 2017, **1**, 1-13.
3. D. Zhang, J. Z. Soo, H. H. Tan, C. Jagadish, K. Catchpole and S. K. Karuturi, *Advanced Energy and Sustainability Research*, 2021, **2**, 2000071.
4. V. Vij, S. Sultan, A. M. Harzandi, A. Meena, J. N. Tiwari, W.-G. Lee, T. Yoon and K. S. Kim, *Acs Catalysis*, 2017, **7**, 7196-7225.
5. Y. Li, X. Bao, D. Chen, Z. Wang, N. Dewangan, M. Li, Z. Xu, J. Wang, S. Kawi and Q. Zhong, *ChemCatChem*, 2019, **11**, 5913-5928.
6. Z. Wang, J. Fan, B. Cheng, J. Yu and J. Xu, *Materials Today Physics*, 2020, 100279.
7. X. Zheng, X. Han, Y. Zhang, J. Wang, C. Zhong, Y. Deng and W. Hu, *Nanoscale*, 2019, **11**, 5646-5654.
8. Y. Yan, B. Y. Xia, B. Zhao and X. Wang, *Journal of Materials Chemistry A*, 2016, **4**, 17587-17603.
9. S. Trasatti, *Journal of Electroanalytical Chemistry and Interfacial Electrochemistry*, 1972, **39**, 163-184.
10. J. Greeley, J. K. Nørskov, L. A. Kibler, A. M. El‐Aziz and D. M. Kolb, *ChemPhysChem*, 2006, **7**, 1032-1035.
11. B. Liu, B. He, H. Q. Peng, Y. Zhao, J. Cheng, J. Xia, J. Shen, T. W. Ng, X. Meng and C. S. Lee, *Advanced Science*, 2018, **5**, 1800406.
12. F. Song, W. Li, J. Yang, G. Han, P. Liao and Y. Sun, *Nature communications*, 2018, **9**, 1-10.
13. W. Hua, H. Sun, H. Liu, Y. Li and J.-G. Wang, *Applied Surface Science*, 2021, **540**, 148407.

14. W. F. Chen, K. Sasaki, C. Ma, A. I. Frenkel, N. Marinkovic, J. T. Muckerman, Y. Zhu and R. R. Adzic, *Angewandte Chemie International Edition*, 2012, **51**, 6131-6135.
15. M. Shalom, D. Ressnig, X. Yang, G. Clavel, T. P. Fellinger and M. Antonietti, *Journal of Materials Chemistry A*, 2015, **3**, 8171-8177.
16. P. J. Kelly and R. D. Arnell, *Vacuum*, 2000, **56**, 159-172.
17. J. Liang, Q. Liu, T. Li, Y. Luo, S. Lu, X. Shi, F. Zhang, A. M. Asiri and X. Sun, *Green Chemistry*, 2021, **23**, 2834-2867.
18. D. Zhang, L. Meng, J. Shi, N. Wang, S. Liu and C. Li, *Electrochimica Acta*, 2015, **169**, 402-408.
19. L. Chen and Q. Xu, *Science*, 2020, **367**, 737-737.
20. J. Li, C. Shu, C. Liu, X. Chen, A. Hu and J. Long, *Small*, 2020, **16**, 2001812.
21. Z. Luo, T. Wang and J. Gong, *Chemical Society Reviews*, 2019, **48**, 2158-2181.
22. D. Zhang, J. Shi, W. Zi, P. Wang and S. Liu, *ChemSusChem*, 2017, **10**, 4324-4341.
23. S. K. Karuturi, H. Shen, A. Sharma, F. J. Beck, P. Varadhan, T. Duong, P. R. Narangari, D. Zhang, Y. Wan and J. H. He, *Advanced Energy Materials*, 2020, **10**, 2000772.
24. B. Ouyang, Y. Zhang, Z. Zhang, H. J. Fan and R. S. Rawat, *Small*, 2017, **13**, 1604265.
25. J. S. Kang, M.-A. Park, J.-Y. Kim, S. H. Park, D. Y. Chung, S.-H. Yu, J. Kim, J. Park, J.-W. Choi and K. J. Lee, *Scientific reports*, 2015, **5**, 1-11.
26. D. Kuznetsov, G. Ugodnikov and I. Filatov, *Technical Physics Letters*, 2008, **34**, 87-89.
27. N. E. Brese and M. O'Keeffe, *Complexes, clusters and crystal chemistry*, 1992, 307-378.
28. K. Xu, P. Chen, X. Li, Y. Tong, H. Ding, X. Wu, W. Chu, Z. Peng, C. Wu and Y. Xie, *Journal of the American Chemical Society*, 2015, **137**, 4119-4125.
29. M.-S. Balogun, Y. Zeng, W. Qiu, Y. Luo, A. Onasanya, T. K. Olaniyi and Y. Tong, *Journal of Materials Chemistry A*, 2016, **4**, 9844-9849.
30. D. Zhang, J. Shi, Y. Qi, X. Wang, H. Wang, M. Li, S. Liu and C. Li, *Advanced Science*, 2018, **5**, 1801216.
31. T. Liu, M. Li, C. Jiao, M. Hassan, X. Bo, M. Zhou and H.-L. Wang, *Journal of Materials Chemistry A*, 2017, **5**, 9377-9390.
32. D. Gao, J. Zhang, T. Wang, W. Xiao, K. Tao, D. Xue and J. Ding, *Journal of Materials Chemistry A*, 2016, **4**, 17363-17369.
33. S. H. Park, Y.-H. Cho, M. Choi, H. Choi, J. S. Kang, J. H. Um, J.-W. Choi, H. Choe and Y.-E. Sung, *Surface and Coatings Technology*, 2014, **259**, 560-569.
34. Y. Wang, Z.-W. Fu, X.-L. Yue and Q.-Z. Qin, *Journal of the Electrochemical Society*, 2004, **151**, E162.
35. L. Xu, Q. Jiang, Z. Xiao, X. Li, J. Huo, S. Wang and L. Dai, *Angewandte Chemie*, 2016, **128**, 5363-5367.
36. E. Rohaeti and I. Hikmawati, *Journal Material Science and Technology*, 2010.
37. H. Ang, H. T. Tan, Z. M. Luo, Y. Zhang, Y. Y. Guo, G. Guo, H. Zhang and Q. Yan, *Small*, 2015, **11**, 6278-6284.
38. S. Geng, F. Tian, M. Li, X. Guo, Y. Yu, W. Yang and Y. Hou, *Journal of Materials Chemistry A*, 2021, **9**, 8561-8567.
39. B. S. Mun, M. Watanabe, M. Rossi, V. Stamenkovic, N. M. Markovic and P. N. Ross Jr, *The Journal of chemical physics*, 2005, **123**, 204717.
40. Y. Pan, K. Sun, Y. Lin, X. Cao, Y. Cheng, S. Liu, L. Zeng, W.-C. Cheong, D. Zhao and K. Wu, *Nano Energy*, 2019, **56**, 411-419.
41. F. Le Formal, M. Grätzel and K. Sivula, *Advanced Functional Materials*, 2010, **20**, 1099-1107.
42. Y. Zheng, Y. Jiao, Y. Zhu, L. H. Li, Y. Han, Y. Chen, A. Du, M. Jaroniec and S. Z. Qiao, *Nature communications*, 2014, **5**, 1-8.
43. N. Krstajić, M. Popović, B. Grgur, M. Vojnović and D. Šepa, *Journal of Electroanalytical Chemistry*, 2001, **512**, 16-26.

44.   W.-F. Chen, J. T. Muckerman and E. Fujita, *Chemical communications*, 2013, **49**, 8896-8909.
45.   Y. Yoon, B. Yan and Y. Surendranath, *Journal of the American Chemical Society*, 2018, **140**, 2397-2400.
46.   J. K. Nørskov, T. Bligaard, A. Logadottir, J. Kitchin, J. G. Chen, S. Pandelov and U. Stimming, *Journal of The Electrochemical Society*, 2005, **152**, J23.
47.   J. Greeley, T. F. Jaramillo, J. Bonde, I. Chorkendorff and J. K. Nørskov, *Nature materials*, 2006, **5**, 909-913.
48.   K. S. Exner, *Angewandte Chemie International Edition*, 2020, **59**, 10236-10240.
49.   H. Li and K. Reuter, *ACS catalysis*, 2020, **10**, 11814-11821.
50.   Z. Liu, S. D. Sajjad, Y. Gao, H. Yang, J. J. Kaczur and R. I. Masel, *International Journal of Hydrogen Energy*, 2017, **42**, 29661-29665.